Published on 11 January 2016. Downloaded by HK University of Science and Technology on 23/03/2018 06:13:55.

Nanoscale

PAPER

View Article Online
View Journal | View Issue

Cite this: *Nanoscale*, 2016, **8**, 6393

Designing nanobowl arrays of mesoporous TiO_2 as an alternative electron transporting layer for carbon cathode-based perovskite solar cells†

Xiaoli Zheng,‡[a] Zhanhua Wei,‡[a] Haining Chen,[a] Qianpeng Zhang,[b] Hexiang He,[c] Shuang Xiao,[d] Zhiyong Fan,[b] Kam Sing Wong[c] and Shihe Yang*[a,d]

Received 28th September 2015,
Accepted 8th January 2016

DOI: 10.1039/c5nr06715d

www.rsc.org/nanoscale

In this work, we have designed a mesoporous TiO_2 nanobowl (NB) array with pore size, bowl size and film thickness being easily controllable by the sol–gel process and the polystyrene (PS) template diameter. Based on the TiO_2 NB array, we fabricated carbon cathode based perovskite solar cells (C-PSCs) to investigate the impact of TiO_2 NB nanostructures on the performance of the as-obtained C-PSCs devices. As expected, the TiO_2 NB based devices show a higher power conversion efficiency (PCE) than that of the planar counterpart, mainly due to the enhanced light absorption arising from the NB-assisted light management, the improved pore-filling of high quality perovskite crystals and the increased interface contact for rapid electron extraction and fast charge transport. Leveraging these advantages of the novel TiO_2 NB film, the 220 nm-PS templated TiO_2 NB based devices performed the best on both light absorption capability and charge extraction, and achieved a PCE up to 12.02% with good stability, which is 37% higher than that of the planar counterpart. These results point to a viable and convenient route toward the fabrication of TiO_2 ETL nanostructures for high performance PSCs.

1. Introduction

Organic–inorganic lead halide perovskite-based mesoscopic or planar heterojunction (PHJ) solar cells have experienced an overwhelming surge in power conversion efficiency (PCE) in the past few years due to their superior photovoltaic properties such as broad light absorption spectra range, high extinction coefficient, long charge-carrier diffusion length, and ambipolar transport.[1–12] Recently, with a suitable work function and electrical conductivity, cheap and abundant carbon materials were successfully used for the cathodes for hole transport material (HTM)-free perovskite solar cell (C-PSCs), and opened up a new era for low-cost, high efficiency PSCs.[13–15] Aside from the low-cost as a result of the elimination of HTM and noble metal and the simplification of device fabrication, the C-PSCs also have the potential to overcome the moisture sensitive bottleneck of the halide perovskites thanks to the hydrophobic properties and the good stability of carbon materials.[16–21] However, the replacement of HTM and metal electrode with the carbon materials hinges on the resolution of some of the current problems involving the nanomaterials and interface engineering. First among the problems is the relatively slow hole extraction, which leads to increased charge recombination and thus low open-circuit voltage (V_{oc}).[13] Second, the low light harvesting efficiency (low IPCE) in the long wavelength range from 500 to 800 nm (for methylammonium lead iodide, $MAPbI_3$) turns up as a key issue because of the absence of light back-scattering from metal electrodes and the insufficient charge separation at low photon energies.[22–25] Therefore, it is urgent to engineer nanomaterials and interfaces to optimize the performance of C-PSCs while retaining their distinct advantages of low cost, good stability and simple fabrication process.

In the meantime, the improvements of C-PSCs have been mainly propelled by working up the device architectures,[26–28] carbon electrode materials and interfaces,[29–33] perovskite crystal quality and compositions,[34–36] and electron transporting layer (ETL) structures and interfaces.[37–39] It is widely recognized that the optical and electronic properties of the ETLs as well as the ETL/perovskite interface are of importance for the

[a]*Department of Chemistry, The Hong Kong University of Science and Technology, Clear Water Bay, Kowloon, Hong Kong, China*
[b]*Department of Electronic and Computer Engineering, The Hong Kong University of Science and Technology, Clear Water Bay, Kowloon, Hong Kong, China*
[c]*Department of Physics, The Hong Kong University of Science and Technology, Clear Water Bay, Kowloon, Hong Kong, China*
[d]*Nano Science and Technology Program, The Hong Kong University of Science and Technology, Clear Water Bay, Kowloon, Hong Kong, China. E-mail: chsyang@ust.hk*
†Electronic supplementary information (ESI) available: Experimental details; text, tables and figures giving detailed and additional material characterization. See DOI: 10.1039/c5nr06715d
‡These authors contributed equally to this work.

Published on 11 January 2016. Downloaded by HK University of Science and Technology on 23/03/2018 06:13:55.

efficiency of PSCs.[40,41] Until now, mesoporous TiO_2 nanoparticle films are the most commonly used ETLs, which serve as a scaffold to support the perovskite layer and facilitate the interfacial charge transfer and the following charge transport, and thereby have enabled by far the best device performance with reduced hysteresis.[9,42,43] Intriguingly, the PSC efficiency is strongly related to the thickness of the TiO_2 scaffold layer: a thick TiO_2 film can scaffold a thick perovskite absorber layer with strong light absorption.[42,44,45] However, a thick TiO_2 film also means numerous interfaces and strong carrier recombination, which would encumber the perovskite pore-filling and slow down charge collection.[46] Conversely, a thin TiO_2 film results in good charge transport but poor light harvesting.[47] Moreover, PSCs based on ultrathin TiO_2 films in terms of the PHJ structure have shown large hysteresis, highlighting the need for predictive control over the perovskite film morphology.[22]

In order to balance the fast charge transport and efficient light harvesting, herein we have designed a TiO_2 nanobowl (TiO_2 NB) array film as an alternative ETL for C-PSCs. The TiO_2 nanobowl (TiO_2 NB) array film was fabricated by combining the colloidal template and liquid phase deposition methods. The resulting TiO_2 NB array film is ordered and offers flexible dimensional and thickness control by changing the polystyrene (PS) diameter in the monolayer packing of PS spheres and the sol–gel processing conditions. Enhanced PCE was obtained due to the predominant role of the TiO_2 NB structure in promoting light harvesting,[48–53] increasing surface area, and improving perovskite crystalline quality. Moreover, the macroporous structure with hollow NB allowed perovskite to easily penetrate into the ETL and thus form an intimate perovskite/TiO_2 interface, which, together with the specially prepared thin compact TiO_2 film, facilitates the charge separation and transport. We have systematically studied the TiO_2 film parameters on the photovoltaic performance, and achieved up to 12.02% PCEs, underpinning the TiO_2 NB array film as a promising perovskite host for understanding the structure–performance relationship of C-PSCs in depth and for applying C-PSCs into commercially viable devices.

2. Results and discussion

Fig. 1 schematizes the process for the synthesis of C-PSCs based on monolayer TiO_2 NB ETL, which was prepared by the PS-template method. As shown, the monolayer TiO_2 NB film was templated straightforwardly by ordered PS arrays, which were fabricated as mono- or bi-layer films on a compact TiO_2 coated FTO substrate *via* the solvent-evaporation-induced self-assembly method (Fig. S1 and S2, ESI†). Subsequently, the macroporous PS arrays were filled with mesoporous TiO_2 by a liquid phase deposition method at room temperature (step 1), forming a monolayer TiO_2 NB film with dual porosity after slow calcination (step 2). Herein, different pore sizes and thicknesses of TiO_2 NB films were fabricated by introducing various diameters of PS spheres (180 nm, 220 nm, 500 nm, Fig. S2†).

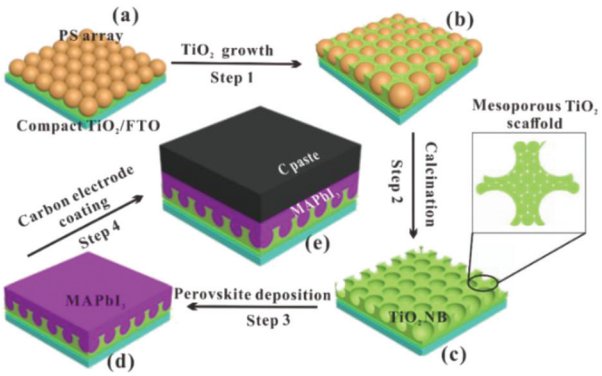

Fig. 1 Schematic fabrication procedure for the TiO_2 NB array film based C-PSCs. (a) PS monolayer; (b) PS monolayer filled with TiO_2 sol; (c) TiO_2 NB array film; (d) perovskite filled and topped TiO_2 NB array; (e) the wrought C-PSC.

Onto the porous TiO_2 NB films, the $CH_3NH_3PbI_3$ ($MAPbI_3$) perovskite was then deposited by a modified two-step solution method (step 3). Finally, carbon (C) paste was directly coated on the perovskite film *via* doctor-blading, thus averting the extra deposition of expensive HTM and noble metal electrode (step 4). For convenience, hereafter, we designate various TiO_2 NB structures as "TiO_2 NB-*x*-P", where *x* refers to the diameters (nm) of the PS template and P represents deposition of perovskite $MAPbI_3$. More experimental details about the TiO_2 NB film formation and device fabrication procedure are given in the ESI† (Experimental methods).

2.1. Formation of TiO_2 NB array

The liquid phase deposition method was used to prepare the TiO_2 NB films through reactions of ammonium hexafluorotitanate ($(NH_4)_2TiF_6$, 0.05 M) and boric acid (H_3BO_3, 0.15 M) within PS array templates.[54,55] More specifically, the deposition reactions can be expressed as:

$$TiF_6^{2-} + 2H_2O \rightarrow TiO_2(s) + 4HF + 2F^- \quad (1)$$

$$H_3BO_3 + 4HF \rightarrow BF_4^- + 3H_2O + H^+ \quad (2)$$

Here the H_3BO_3 serves as an F^- scavenger (eqn (2)) and thus accelerates the hydrolysis reaction (eqn (1)). In this way, the TiO_2 film thickness can be easily controlled by the reaction time and PS diameters.

Fig. 2 shows scanning electron microscopy (SEM) images of the as-obtained monolayer ordered TiO_2 NB arrays along with a planar TiO_2 film for comparison. Clearly, the TiO_2 films prepared by the liquid phase deposition method are all composed of mesoporous TiO_2 nanoparticles with a size of 20–25 nm (Fig. 2 and enlarged SEM image shown in Fig. S3†). The diameters of the individual TiO_2 NBs are found to be 160 nm, 200 nm, and 470 nm with a 25–50 nm connective vein for TiO_2 NB-180, TiO_2 NB-220, and TiO_2 NB-500, respectively. The decreased diameters of the TiO_2 NB compared to the PS templates can be ascribed to the volume shrinking during the cal-

 This journal is © The Royal Society of Chemistry 2016

Published on 11 January 2016. Downloaded by HK University of Science and Technology on 23/03/2018 06:13:55.

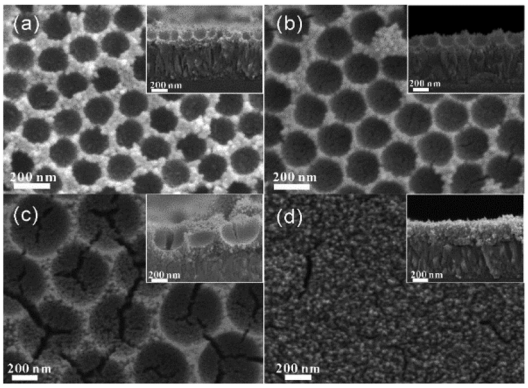

Fig. 2 Top-view and the corresponding cross-sectional SEM images (insets) of (a) TiO_2 NB-180, (b) TiO_2 NB-220, (c) TiO_2 NB-500, and (d) planar TiO_2.

cination process. Cross-sectional SEM characterization (insets) testifies the uniform distribution of monolayer TiO_2 NBs and the good connection with the compact TiO_2 coated on FTO. The heights of the monolayer TiO_2 NBs are 150 nm, 180 nm, and 300 nm, each on a 75 nm compact layer, for TiO_2 NB-180, TiO_2 NB-220, and TiO_2 NB-500, respectively, which are uniformly smaller than the corresponding NB diameters, especially for larger NBs, due to gravity enhanced vertical shrinking. For comparison, a planar TiO_2 film 240 nm thick was also prepared on an identical TiO_2 compact layer by the same procedure but without the PS template (Fig. 2d). It should be pointed out that cracks are clearly observed in the films, especially in the TiO_2 NB-500 and planar TiO_2 films, that is, when the films become thick. The cracks are caused by the stress generated during the growth and calcination processes, which increases with the film thickness. Actually, to our advantage, the presence of NBs decreases the effective TiO_2 film thickness, which would lessen the cracking, and the open hemisphere-like structure increases the effective perovskite/TiO_2 interface area, which would ease the full-filling of perovskite crystals thus facilitating the charge separation/transport.

2.2. Perovskite and carbon electrode deposition

The synthesized TiO_2 NB films were then used for the deposition of $MAPbI_3$. As shown in Fig. 3a–d, the $MAPbI_3$ perovskite densely covers the entire TiO_2 film with a capping layer of about 400–500 nm. Top-view SEM images (Fig. S4a–d†) also show that dense and uniform perovskite crystals with a size of 100–250 nm have been deposited on the TiO_2 NB architectures, whereas obvious pinholes (shown by white dotted circles in Fig. S4d†) can be found in the planar TiO_2 sample. To understand better how the TiO_2 NB films influence the perovskite crystals grown above, we also monitored the morphologies of the PbI_2 films deposited on the TiO_2 NB-220 and planar TiO_2 films by SEM (Fig. S5†). Noticeably, a large and dense PbI_2 crystal layer with a thickness of ~310 nm (capping layer) was formed on the TiO_2 NB-220 film, whereas a thinner PbI_2

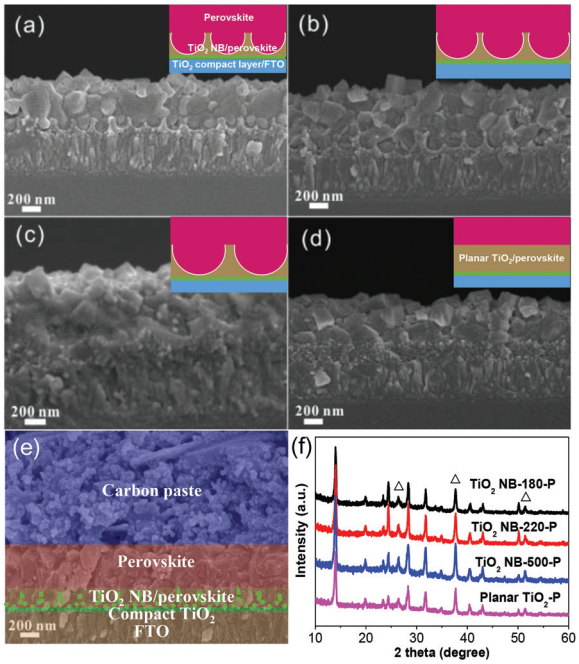

Fig. 3 Cross-sectional SEM images of (a) TiO_2 NB-180-P, (b) TiO_2 NB-220-P, (c) TiO_2 NB-500-P, and (d) planar TiO_2-P. The corresponding schematic diagrams in the insets of (a–d) show the structures of perovskite-deposited TiO_2 films. (e) Cross-sectional SEM image of C-PSC device based on TiO_2 NB-220-P. (f) XRD patterns of perovskite deposited on different TiO_2 films. Δ represents the XRD peaks of FTO.

capping layer (~260 nm) with obvious pinholes was formed on the planar TiO_2 film. It has been well established that a high quality PbI_2 film is a prerequisite for growing a dense and highly crystalline perovskite layer.[56] Thus the dense PbI_2 and perovskite films with a full coverage on the TiO_2 NB film indicate that the surface patterned TiO_2 NB film could serve as a good scaffold for growing the uniform PbI_2 capping layer and thus for facilitating the formation of the dense perovskite crystalline layer.[57] Moreover, the open macropores of TiO_2 NB can promote intimate TiO_2/perovskite interface formation, whereas the small interface in the planar TiO_2 film appears to be insufficient to guide the crystal growth of the perovskite, thus resulting in the pinhole formation. Understandably, controlling the crystal growth of the perovskite has a significant impact on the charge carrier mobility and interfacial charge separation rate.[58,59] Thanks to the uniform perovskite crystals, they can form an intimate interface with the carbon cathode without obvious gaps (Fig. 3e).

The compositions of the perovskite films on TiO_2 NB and planar substrates were investigated by X-ray diffraction (XRD). As shown in Fig. 3f, the strong Bragg peaks at 14.03°, 28.37°, 31.79°, and 43.10° can be assigned respectively to (110), (220), (310), and (330) of $MAPbI_3$, which are subsumed in the tetragonal phase.[25] Unlike the conventional two-step method reported previously, the MAI (1 mg ml^{-1}) in cyclohexane (CHex)/isopropanol (IPA) = 9/1 (v/v) mixed solvent was used to convert the pre-formed lead iodide (PbI_2) film into perovskite.

Published on 11 January 2016. Downloaded by HK University of Science and Technology on 23/03/2018 06:13:55.

In the mixed solution, the "Ostwald ripening" effect of $MAPbI_3$ crystal can be effectively suppressed by the cyclohexane which acts as an antisolvent to allow controlled crystallization at a low concentration of MAI. SEM images and XRD patterns of the $MAPbI_3$ perovskite film prepared by a conventional sequential solution method using pure IPA are also shown in Fig. S6† for comparison. Obviously, the crystal sizes of the pure IPA deposited $MAPbI_3$ vary greatly from 70–100 nm of small crystals to 500–600 nm of large crystals; the large crystals protrude out from the film, which are much larger than those prepared from the CHex/IPA mixed solvent (100–250 nm). The large crystals protruding out of the film would result in the formation of apparent gaps at the interface of the carbon electrode and perovskite (Fig. S6f†). Meanwhile, on comparing the XRD patterns, we notice a characteristic peak of PbI_2 at 12.50° for the pure IPA deposited perovskite film (Fig. S6g†), indicating the incompletely converted PbI_2 even with a high concentration of MAI.[60] In contrast, the absence of the peak of PbI_2 at 12.50° for the CHex/IPA mixed solvent deposited perovskite film connotes the complete conversion of PbI_2, which is auspicious for high photoelectronic performance.

2.3. Photovoltaic performance

Fig. 4 shows photovoltaic performance characteristics of four representative C-PSCs based on the TiO_2 NBs and planar TiO_2 films. The photocurrent–voltage (J–V) curves of the C-PSCs shown in Fig. 4a were measured under standard global AM 1.5, 100 mW cm^{-2} light illumination, and the measured parameters are summarized in Table 1. Obviously, devices based on TiO_2 NB show higher efficiency than that based on the planar TiO_2 film, and in more detail, one notices a dependence of the TiO_2 NB size on photovoltaic performance. The highest PCE of 12.02% was achieved for the TiO_2 NB-220-P based C-PSC, with an open-circuit voltage (V_{oc}) of 1.00 V, a short-circuit current density (J_{sc}) of 22.67 mA cm^{-2} and a fill factor (FF) of 0.53. Notably, the PCE improvement for TiO_2 NB based C-PSCs, with increased J_{sc}, V_{oc}, and FF, especially J_{sc}, stems for the most part from the improved perovskite/TiO_2 interface and the increased light harvesting efficiency due to the unique architecture of the TiO_2 NB arrays. The different performance of the TiO_2 NB based C-PSCs might result from the varied pore sizes and film thicknesses, which might influence the perovskite crystal deposition and thus the charge transport and light management properties. As evidently demonstrated by the dark J–V curves in Fig. 4a, devices fabricated from TiO_2 NB show a much higher dark current onset than that of the planar TiO_2 film based device. This is indicative of effectively inhibited charge recombination in the TiO_2 NB based devices.[25] To further check the reproducibility of the PSCs, the histograms of the V_{oc}, J_{sc}, FF and PCE for a batch of 20 devices based on TiO_2 NB-180-P, TiO_2 NB-220-P, TiO_2 NB-500-P and planar TiO_2-P are shown in Fig. S7† and the statistics are summarized in Table S1.† The small standard deviations indicate good device reproducibility. For comparison, TiO_2 NB-220-P based C-PSCs with the conventional pure IPA solution deposited perovskite film were also prepared, and the optimized device gave a V_{oc} of 0.98 V, a J_{sc} of 21.59 mA cm^{-2}, a FF of 0.51, and a PCE of 10.79% (Fig. S8†), showing an inferior photovoltaic performance than that prepared with the mixed CHex/IPA solvent (12.02%). The incomplete PbI_2 conversion and inferior perovskite/carbon interface could therefore be the explanation for the significantly decreased PV performance.

Table 1 PV performances of C-PSCs based on TiO_2 NB architectures with varied pore sizes and planar TiO_2 for comparison

Samples	V_{oc} (V)	J_{sc} (mA cm^{-2})	FF	PCE (%)	Integrated J_{sc} [a] (mA cm^{-2})
TiO_2 NB-180-P	0.98	21.80	0.53	11.32	19.82
TiO_2 NB-220-P	1.00	22.67	0.53	12.02	20.71
TiO_2 NB-500-P	0.98	20.18	0.51	10.09	18.41
Planar TiO_2-P	0.97	18.07	0.50	8.76	17.38

[a] Integrated J_{sc} from the IPCE curves shown in Fig. 4b.

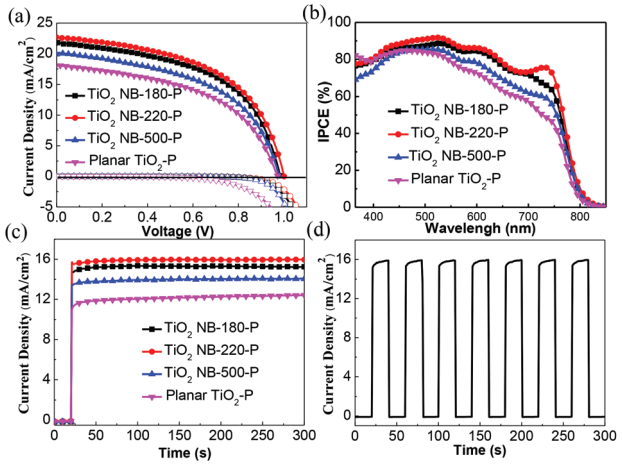

Fig. 4 Comparison of the photovoltaic performance of the C-PSCs devices based on different TiO_2 films. (a) Characteristic J–V and dark J–V plots, and (b) the IPCE spectra of the C-PSCs devices based on different TiO_2 films. (c) Photocurrent density as a function of time for the devices held at the maximum output power point (0.73 V, 0.74 V, 0.70 V and 0.69 V for TiO_2 NB-180-P, TiO_2 NB-220-P, TiO_2 NB-500-P, and planar TiO_2-P, respectively). (d) Photocurrent density as a function of time held at the maximum output power point (0.74 V) under on–off illumination cycles for TiO_2 NB-220-P based C-PSC.

Fig. 4b shows incident-photon-to-current conversion efficiency (IPCE) spectra for the four representative C-PSCs based on TiO_2 NB and planar TiO_2. Like most of the reported C-PSCs, the planar TiO_2-P based cell exhibits IPCE values of above 80% at <550 nm and decreases dramatically in the long wavelength range. The use of TiO_2 NB arrays brings in a noticeable IPCE improvement in the long wavelength range of 500–760 nm, mainly due to the increased effective light harvesting and/or charge extraction, which will be discussed below.[61] This IPCE enhancement correlates well with the higher photocurrent in the TiO_2 NB based C-PSCs. Integrating the overlap of the IPCE spectrum yield a photocurrent density

 This journal is © The Royal Society of Chemistry 2016

Published on 11 January 2016. Downloaded by HK University of Science and Technology on 23/03/2018 06:13:55.

of 19.82, 20.71, 18.41, and 17.38 mA cm^{-2} for TiO_2 NB-180-P, TiO_2 NB-220-P, TiO_2 NB-500-P and planar TiO_2-P, which are in excellent agreement with the measured photocurrent density (Fig. 4a and Table 1). It has been widely recommended that monitoring the stabilized current density at the maximum output power point is a useful parameter to present the cell performance alongside the *J–V* scan derived PCE.[25,62] We thus recorded the photocurrent density of the four representative C-PSCs based on TiO_2 NB and planar TiO_2 at a function of time held at the maximum output power point (Fig. 4c). As shown in Fig. 4c, the photocurrent density of the devices based on TiO_2 NB arrays stabilize quickly within seconds and yield a stabilized PCE around 11.13%, 11.80%, and 9.82% for TiO_2 NB-180-P, TiO_2 NB-220-P, and TiO_2 NB-500-P, respectively, measured 300 s after. However, a continuous increase of the photocurrent density is observed for the planar TiO_2-P based C-PSC yielding a stabilized PCE of around 8.57%; the lower performance could originate from the inferior perovskite/TiO_2 interface, such as the one with pinholes mentioned above.

In addition, the photocurrent density-time profile at the maximum output power point under on-off illumination cycles for TiO_2 NB-220-P based C-PSC was recorded (Fig. 4d) and a fast photo-response to light on and off is evident, indicating the fast electron transfer due to the intimate interface of TiO_2 NB-220-P/perovskite. The stability of the champion TiO_2 NB-220-P based C-PSC under ambient conditions was also investigated (Fig. S9†). Significantly, only a slight PCE decrease was observed for the champion C-PSC; the PCE decline was from 12.02% to 11.09% with an 8% drop after 45 days' storage without any encapsulation (humidity 10–20%), indicating a good stability of the C-PSCs mainly due to the high quality of perovskite crystalline films, intimate interface between the perovskite and TiO_2 NB and the compact carbon electrode.[17] Moreover, to detect any hysteresis in the devices, the *J–V* curves of the C-PSCs based on different TiO_2 films were further measured *via* the forward and backward scans with a scan rate of 10 mV s^{-1}. Obviously, the TiO_2 NB films based C-PSCs, especially the TiO_2 NB-220-P based C-PSC, show smaller hysteresis than the planar TiO_2 film based C-PSCs (Fig. S10†). The origin of the *I–V* hysteresis has been widely studied, and the degree of hysteresis strongly depends on the quality of the perovskite and the mesoporous TiO_2 layers as well as their interface.[62] Considering that these four C-PSCs have a similar cell configuration and used the same perovskite deposition method, it is believed that the different performance with respect to the hysteresis effect is due to the different interface quality of the TiO_2/perovskite which directly influences the electron transfer and transport processes. By combining the SEM results in Fig. 3 and the hysteresis investigation in Fig. S10,† we submit that the TiO_2 NB array architecture provides a more favorable interface for electron collection.

2.4. Structure–performance correlation – light trapping

For PSCs, multiple factors determine the photovoltaic performance. To understand the origin of the PCE improvement for the TiO_2 NB based C-PSCs, we first examine the optical properties of the devices. For comparison of the light management properties of the TiO_2 NB array film with different pore sizes and the planar film, UV-vis optical properties were measured using an integrating sphere for the propagation of incident light from the glass side. First, the transmittance of ETL-coated FTO substrate could significantly affect the capture of incident light by the perovskite active layer, and was thus carefully measured using FTO as a control sample. Fig. 5a shows the transmittance spectra of TiO_2 NB arrays with varied NB sizes and the planar TiO_2 film on FTO. Interestingly, the transmittance is strongly dependent on the geometry and thickness of the TiO_2 films. Particularly noteworthy is that FTO substrates coated with TiO_2 NB-180 and TiO_2 NB-220 films show better transmittance than the bare FTO over the wavelength ranges of 530–650/730–800 nm and 500–650/750–800 nm, respectively, mainly due to the effective anti-reflective effect of the TiO_2 NB array film.[63,64] The slight transmittance difference between the TiO_2 NB-180 and TiO_2 NB-220 film is because the anti-reflective effect is thickness-dependent.[65,66] Also, it is observed that the transmittance of TiO_2 NB-500 is higher than that of planar TiO_2 especially in the range of 500–800 nm, indicating that the unique geometry of

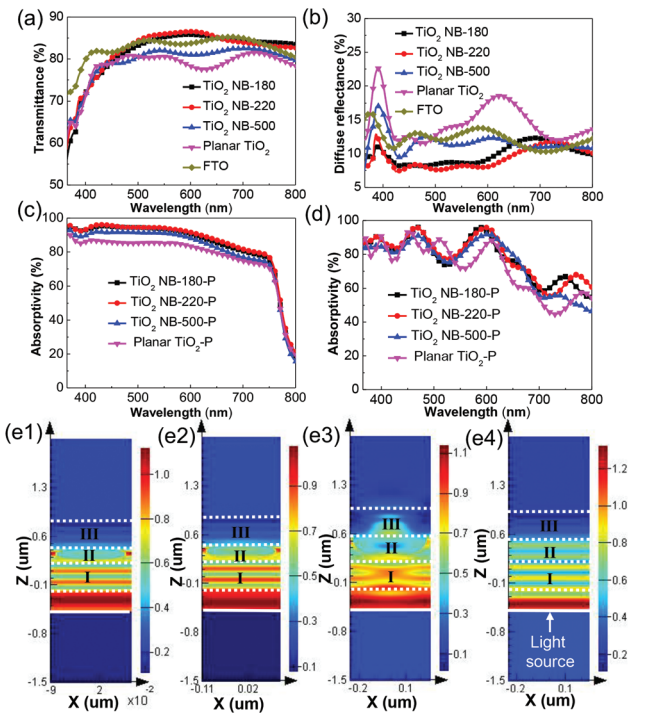

Fig. 5 (a) Optical transmittance spectra and (b) reflectance spectra of different TiO_2 films and FTO, (c) experimental and (d) simulated absorptivity spectra of perovskite films deposited on different TiO_2 films. (e) Simulated cross-sectional |*E*| distribution of the EM wave at 600 nm wavelength in the perovskite deposited (e1) TiO_2 NB-180-P, (e2) TiO_2 NB-220-P, (e3) TiO_2 NB-500-P, and (e4) planar TiO_2-P, the ranges between the white dotted lines represent (I) FTO, (II) TiO_2 compact layer + TiO_2 ETL/perovskite, and (III) perovskite capping layer.

Published on 11 January 2016. Downloaded by HK University of Science and Technology on 23/03/2018 06:13:55.

the TiO_2 NB array can facilitate the light transmittance. However, for the sample of TiO_2 NB-500, the transmittance is decreased between 440–800 nm compared with those of TiO_2 NB-180 and TiO_2 NB-220, probably due to the increased Rayleigh scattering from the TiO_2 nanoparticles for the increased film thickness (insets in Fig. 2).[67]

We next examine the diffuse reflectance spectra of the TiO_2 films shown in Fig. 5b. In general, the TiO_2 NB films exhibit a significant suppression of reflection over a broad spectral range compared with the planar film. The average reflectance of the TiO_2 NB-coated FTO is significantly suppressed to be below 15% throughout the whole wavelength range, especially for the TiO_2 NB-180 and TiO_2 NB-220 films, in agreement with the transmittance results. Such increased transmittance and broadband anti-reflection of the TiO_2 NB array-coated FTO can be ascribed to the light management ability of the unique 3D geometry and the 2D periodic structure. Simply from the classical electrodynamics, the TiO_2 NB array with sub-wavelength features imparts a smooth refractive index transition (the so-called graded refractive index) like the moth-eye, and thereby effectively suppresses light reflection and increases the light transmittance.[65]

To further investigate the light management properties of the TiO_2 NB arrays, absorptivity spectra (A) of the perovskite films on different TiO_2 films were extracted from the measured reflectance (R) and transmittance (T) spectra through the relation of $A = 1 - R - T$ (Fig. S11†). As shown in Fig. 5c, the absorptivity of the TiO_2 NB based perovskite films is remarkably enhanced compared with the planar TiO_2-P, and among them, the TiO_2 NB-180-P and TiO_2 NB-220-P films show a higher broadband absorptivity than the TiO_2 NB-500-P film. Notably, compared to the TiO_2 NB-180-P, TiO_2 NB-220-P presents even higher absorption, mainly due to its superior anti-reflection properties (Fig. 5a,b and S8a,b†), which is held responsible for the J_{sc} enhancement shown in Fig. 4a.

In order to further verify the experimental results, finite-difference-time-domain (FDTD) simulations were performed on these films. Gratifyingly, the simulated absorptivity spectra (Fig. 5d) show a quite consistent trend over all the wavelengths with the experimental counterparts (Fig. 5c). The higher absorptivity above 700 nm in the simulated absorptivity spectra is mainly due to the perfect perovskite film in the simulated model compared with the practical ones, which would lead to lower transmittance and thus higher absorptivity in the long wavelength range (Fig. S11†). In addition, the big oscillation in the simulated absorptivity spectra results from the simulation employing perfect surfaces and interfaces, which lead to constructive and/or destructive interference, in contrast to real experiments wherein the surface and interfaces will be rough.

To shed light on how light is coupled into the films, the cross-sectional electric field intensity ($|E|$) distributions of the electromagnetic (EM) wave at 600 nm are calculated and shown in Fig. 5e. In these simulation models, the EM plane waves propagate upward from $Z = -0.5$ μm and reach the FTO bottom surfaces at $Z = -0.2$ μm. Note that the color index at the specific location in the cross-sectional $|E|$ distribution indicates the magnitude of $|E|$ at that point.[68,69] The refractive index (RI) of perovskite was used according to the literature,[70] and the RI of FTO, TiO_2 compact layer and mesoporous TiO_2 layer were measured by ellipsometry (the RI data of different layers are shown in Fig. S12†). In order to facilitate the observation of light propagation, white dotted lines are used in Fig. 5e1–e4 to show the edges of individual material layers in the devices. The fringe patterns in Fig. 5e above $Z = -0.5$ μm originate from the interference between the light source and the reflected light, and the color index blow $Z = -0.5$ μm indicates the intensity of reflected light.[69] The cross-sectional $|E|$ distributions reveal a lower reflection for the TiO_2 NB-180-P (Fig. 5e1) and TiO_2 NB-220-P (Fig. 5e2) films than the TiO_2 NB-500-P (Fig. 5e3) and planar TiO_2-P (Fig. 5e4) films, as indicated by the darker color below the light source due to their antireflective effects associated with the smaller-sized NB arrays. Interestingly, the color patterns in the II and III regions in Fig. 5e illustrate that the TiO_2 NB array based samples have a much stronger electric field intensity inside the mesoporous TiO_2 ETL layer and the perovskite capping layer than the planar based sample. This is because more incident photons are coupled into the TiO_2 NB array based samples due to their superior antireflection effect, which is beneficial for light absorption by the perovskite absorber to generate charge carriers. However, for the TiO_2 NB-500-P sample, the stronger reflection than that of the TiO_2 NB-180-P and TiO_2 NB-220-P samples results in a lower light absorption, in accordance with the lower J_{sc} as presented in Fig. 4a.

As mentioned above, the combination of optical measurements and simulation investigation has shown the potency of the TiO_2 NB arrays with an appropriate pore size and thickness for photon capturing. Previous studies have demonstrated that TiO_2 NB arrays possess a graded refractive index feature like moth-eye, so incident light rays tend to be bent progressively, effectively suppressing light reflection (Fig. S13-I†)[65,66] and thereby increasing light absorption. From another perspective, as light passes through the periodic TiO_2 NB array, multiple internal reflections increase the effective light path in the active layer, which are more obvious in TiO_2 NB arrays with an NB size comparable to the light wavelength (Fig. S13-II†).[67,71,72] On the other hand, a suitable pore size (pitch) and thickness of TiO_2 NB films should be designed to minimize the light loss through strong backward scattering (predominated by Rayleigh and Mie scattering from nanoparticles and pores).[73–76] The stronger backward scattering could explain the inferior transmittance and anti-reflectance of TiO_2 NB-500-P than that of TiO_2 NB-180-P and TiO_2 NB-220-P due to its larger pore size and film thickness. The slightly better anti-reflectance effect of TiO_2 NB-220-P than that of TiO_2 NB-180-P may also be ascribed to the appropriate film thickness that can optimize light bending without very strong back scattering effect.[65] Therefore, a periodic TiO_2 NB array structure with an appropriate pore size and film thickness in the front of a device can reduce reflection losses and thus effectively enhance the light absorption in the active layer, leading to improved J_{sc}.

 This journal is © The Royal Society of Chemistry 2016

Published on 11 January 2016. Downloaded by HK University of Science and Technology on 23/03/2018 06:13:55.

2.5. Structure–performance correlation – charge transfer

For different TiO_2 architecture based C-PSCs, the capability of extracting electrons through the perovskite/TiO_2 interface is also of great importance for the photovoltaic performance. Thus, the electron transfer kinetics were evaluated by means of time-resolved photoluminescence (TRPL) characterization.[8,77] Fig. 6a shows the room temperature TRPL profiles of perovskite deposited on TiO_2 NB arrays and planar TiO_2. Note that there is no carbon electrode in these films so that we can focus on the perovskite/TiO_2 interface. The PL decays were fitted by global bi-exponential model and the detailed fitted PL lifetimes (τ_1, τ_2, and τ) are collected in Table 2.[78,79] For simplicity, the weighted average value of τ_1 and τ_2 is utilized to represent the PL lifetime (τ, Table 2). As illustrated in Fig. 6a, an enhanced PL quenching rate is observed with the TiO_2 NBs, and the fitted PL lifetime follows the sequence as τ (TiO_2 NB-220-P) < τ (TiO_2 NB-180-P) < τ (TiO_2 NB-500-P) < τ (planar TiO_2-P). The PL quenching rate is expected to originate from the charge-carrier extraction across the interface, and it suggests that the photoinduced electrons in perovskite could be more efficiently extracted by the TiO_2 NB arrays due to their increased interfacial area and contact with perovskite.[77] Presumably, for TiO_2 NB-220-P, the appropriate TiO_2 film thickness and pore size could have contributed to the efficient electron extraction by promoting the quality of the perovskite deposition and the interface contact. In short, the high PCE of the TiO_2 NBs based C-PSCs results not only from the enhanced light-management properties but also from the enhanced charge extraction stemming from the unique 3D NB array architecture.

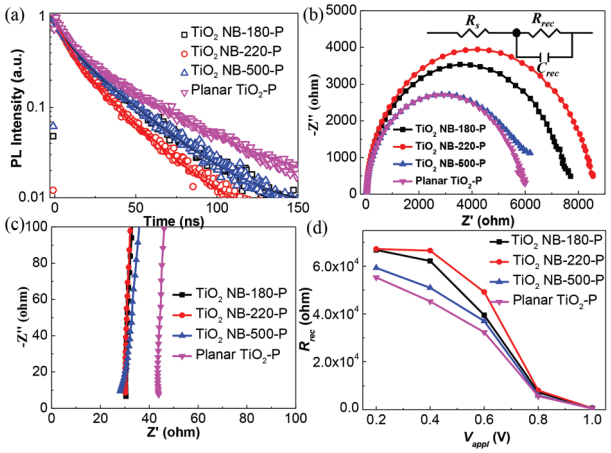

Fig. 6 (a) Time-resolved PL measurements taken at the peak emission wavelength of perovskite deposited upon different TiO_2 films after excitation at 400 nm (3.8 MHz, 55 μW). The solid lines in (a) are the biexponential fits of the PL decay transients. (b, c) Nyquist plots of C-PSCs based on different TiO_2 films in the dark at a bias voltage of 0.8 V, equivalent circuit is in the inset of (b). (d) Recombination resistance (R_{rec}) as a function of applied bias voltage (V_{appl}) curves for C-PSCs based on different TiO_2 films.

Table 2 Fitted PL lifetimes (τ_1, τ_2, and τ) of perovskite deposited upon different TiO_2 films, and the fitting parameters, series resistance (R_s) and recombination resistance (R_{rec}), obtained from EIS data using the equivalent circuit in Fig. 6b

Samples	τ_1 [a] (ns)	τ_2 [a] (ns)	τ [a] (ns)	R_s (ohm)	R_{rec} (ohm)
TiO_2 NB-180-P	6.2	28.4	19.0	30.0	7300
TiO_2 NB-220-P	6.0	23.6	15.1	29.5	8100
TiO_2 NB-500-P	7.1	28.9	19.6	27.2	5980
Planar TiO_2-P	7.1	38.3	22.7	42.5	5680

[a] The PL lifetimes (τ_1, τ_2, and τ) are fitted by the biexponential model: $y = A_1 \times \exp(x/\tau_1) + A_2 \times \exp(x/\tau_2)$, A_1 and A_2 are the prefactors, τ_1 and τ_2 are the lifetimes of the fast and slow decay component, respectively, and $\tau = A_1/(A_1 + A_2) \times \tau_1 + A_2/(A_1 + A_2) \times \tau_2$.

To gain a deeper insight into the photovoltaic performance improvement by TiO_2 NB structures, we resorted to electrochemical impedance spectroscopy (EIS) characterization, which is a powerful technique for investigating the mechanism of carrier transport and recombination in solar cells.[80] The Nyquist plots for different TiO_2 structure based C-PSCs measured in the dark at a bias voltage of 0.8 V are presented in Fig. 6b and c. The equivalent circuit shown in the inset of Fig. 6b was used for fitting the EIS data and the detailed fitting result is summarized in Table 2. The large semicircle in the low-frequency range was attributed to the recombination resistance (R_{rec}) and capacitance in literature reports, and a higher R_{rec} is associated with a lower carrier recombination.[40] As shown in Fig. 6b, for the cells, R_{rec} follows the sequence of TiO_2 NB-220-P > TiO_2 NB-180-P > TiO_2 NB-500-P > planar TiO_2-P, highlighting the role of TiO_2 NB arrays in abating the carrier recombination. Conceivably, the porous structure of TiO_2 NB arrays would increase the interface area of the perovskite and TiO_2, meaning that excitons or the resulting charge carriers can more easily drift to the interface for charge separation with reduced occurrence of trap-assisted recombination. It should be noted that the transmission line behaviour is not present in the EIS plot before the recombination RC element as in the conventional dye-sensitized solar cells with the relatively thick TiO_2 film (8–12 μm) being the electron pathway.[26,81] This should be mainly due to the much faster electron transport in PSCs resulting from the much thinner meso-layer (150 nm–1.5 μm), the two transport pathways (perovskite layer and TiO_2 layer) and the built-in potential for electron drift, which make the transport time too small to be clearly observed by EIS.[40] Another important parameter, which can be obtained from the EIS from the intersection point of the semicircle with the real axis on the left side, is the series resistance (R_s), which is purportedly affected by the ETL.[80] As shown in Fig. 6c, the R_s values of the cells based on TiO_2 NBs are much lower than that of the planar TiO_2 based device due to the reduced mean thickness of the TiO_2 NB arrays.[82,83]

Fig. 6d plots R_{rec} of different TiO_2 films based C-PSCs as a function of the applied bias voltage (V_{appl}). Notably, the R_{rec} values measured at different V_{appl} follow the same sequence as those measured at 0.8 V, further verifying the suppression of charge recombination in the TiO_2 NB based C-PSCs. Of course, as the bias increases, the R_{rec} monotonically decreases as

Published on 11 January 2016. Downloaded by HK University of Science and Technology on 23/03/2018 06:13:55.

expected. The distinctive charge recombination suppression characteristics of the TiO_2 NB arrays are advantageous for improving V_{oc} and FF values of C-PSCs.[27]

3. Conclusions

In summary, we have developed a facile PS template method to fabricate monolayer ordered TiO_2 NB arrays with varied pore sizes and thicknesses and demonstrated that the TiO_2 NB arrays can serve as efficient ETL for high performance C-PSCs. We have studied the effect of pore sizes and film thicknesses of the TiO_2 NB arrays on the performance of C-PSCs, and the C-PSC based on the TiO_2 NB-220-P array has achieved the highest PCE up to 12.02% with good stability. Through a series of optical characterization, FDTD simulation, TRPL and EIS characterizations, we found that the TiO_2 NB array structure with an optimum pore size and thickness can reduce the reflection losses and thus effectively enhance the light absorption in the active layer. In addition, the open NB structure enhances the quality of the supported perovskite film and increases the interface area between perovskite and TiO_2, which are favorable for charge separation at the interface and the subsequent charge transport, effectively reducing the occurrence of trap-assisted recombination. Taken together, the results establish the TiO_2 NB arrays as a promising perovskite host for enhancing light absorption and charge separation/transport, and as a platform for understanding the structure-dependent-performance of C-PSCs in depth.

Conflict of interest

The authors declare no competing financial interest.

Acknowledgements

This work was supported by the HK Innovation and Technology Fund (ITS/004/14), the NSFC/HK-RGC Joint Research Scheme (N_HKUST 610/14) and the Research Grants Council of Hong Kong (AoE/P-02/12).

References

1 A. Kojima, K. Teshima, Y. Shirai and T. Miyasaka, *J. Am. Chem. Soc.*, 2009, **131**, 6050–6051.
2 H. S. Kim, C. R. Lee, J. H. Im, K. B. Lee, T. Moehl, A. Marchioro, S. J. Moon, R. Humphry-Baker, J. H. Yum, J. E. Moser, M. Gratzel and N. G. Park, *Sci. Rep.*, 2012, **2**, 591.
3 M. Z. Liu, M. B. Johnston and H. J. Snaith, *Nature*, 2013, **501**, 395–398.
4 H. P. Zhou, Q. Chen, G. Li, S. Luo, T. B. Song, H. S. Duan, Z. R. Hong, J. B. You, Y. S. Liu and Y. Yang, *Science*, 2014, **345**, 542–546.
5 D. Y. Liu and T. L. Kelly, *Nat. Photonics*, 2014, **8**, 133–138.
6 S. D. Stranks, G. E. Eperon, G. Grancini, C. Menelaou, M. J. P. Alcocer, T. Leijtens, L. M. Herz, A. Petrozza and H. J. Snaith, *Science*, 2013, **342**, 341–344.
7 Q. F. Dong, Y. J. Fang, Y. C. Shao, P. Mulligan, J. Qiu, L. Cao and J. S. Huang, *Science*, 2015, **347**, 967–970.
8 G. C. Xing, N. Mathews, S. Y. Sun, S. S. Lim, Y. M. Lam, M. Gratzel, S. Mhaisalkar and T. C. Sum, *Science*, 2013, **342**, 344–347.
9 W. S. Yang, J. H. Noh, N. J. Jeon, Y. C. Kim, S. Ryu, J. Seo and S. I. Seok, *Science*, 2015, **348**, 1234–1237.
10 M. M. Lee, J. Teuscher, T. Miyasaka, T. N. Murakami and H. J. Snaith, *Science*, 2012, **338**, 643–647.
11 L. Etgar, P. Gao, Z. S. Xue, Q. Peng, A. K. Chandiran, B. Liu, M. K. Nazeeruddin and M. Gratzel, *J. Am. Chem. Soc.*, 2012, **134**, 17396–17399.
12 J. J. Shi, J. Dong, S. T. Lv, Y. Z. Xu, L. F. Zhu, J. Y. Xiao, X. Xu, H. J. Wu, D. M. Li, Y. H. Luo and Q. B. Meng, *Appl. Phys. Lett.*, 2014, **104**, 063901.
13 A. Y. Mei, X. Li, L. F. Liu, Z. L. Ku, T. F. Liu, Y. G. Rong, M. Xu, M. Hu, J. Z. Chen, Y. Yang, M. Gratzel and H. W. Han, *Science*, 2014, **345**, 295–298.
14 Z. H. Wei, K. Y. Yan, H. N. Chen, Y. Yi, T. Zhang, X. Long, J. K. Li, L. X. Zhang, J. N. Wang and S. H. Yang, *Energy Environ. Sci.*, 2014, **7**, 3326–3333.
15 Y. Y. Yang, J. Y. Xiao, H. Y. Wei, L. F. Zhu, D. M. Li, Y. H. Luo, H. J. Wu and Q. B. Meng, *RSC Adv.*, 2014, **4**, 52825–52830.
16 S. N. Habisreutinger, T. Leijtens, G. E. Eperon, S. D. Stranks, R. J. Nicholas and H. J. Snaith, *Nano Lett.*, 2014, **14**, 5561–5568.
17 Z. H. Wei, X. L. Zheng, H. N. Chen, X. Long, Z. L. Wang and S. H. Yang, *J. Mater. Chem. A*, 2015, **3**, 16430–16434.
18 H. W. Zhou, Y. T. Shi, Q. S. Dong, H. Zhang, Y. J. Xing, K. Wang, Y. Du and T. L. Ma, *J. Phys. Chem. Lett.*, 2014, **5**, 3241–3246.
19 X. Li, M. Tschumi, H. W. Han, S. S. Babkair, R. A. Alzubaydi, A. A. Ansari, S. S. Habib, M. K. Nazeeruddin, S. M. Zakeeruddin and M. Gratzel, *Energy Technol.-Ger.*, 2015, **3**, 551–555.
20 K. Leo, *Nat. Nanotechnol.*, 2015, **10**, 574–575.
21 G. D. Niu, X. D. Guo and L. D. Wang, *J. Mater. Chem. A*, 2015, **3**, 8970–8980.
22 K. C. Wang, J. Y. Jeng, P. S. Shen, Y. C. Chang, E. W. G. Diau, C. H. Tsai, T. Y. Chao, H. C. Hsu, P. Y. Lin, P. Chen, T. F. Guo and T. C. Wen, *Sci. Rep.*, 2014, **4**, 4756.
23 Z. G. Xiao, C. Bi, Y. C. Shao, Q. F. Dong, Q. Wang, Y. B. Yuan, C. G. Wang, Y. L. Gao and J. S. Huang, *Energy Environ. Sci.*, 2014, **7**, 2619–2623.
24 Q. Wang, Y. C. Shao, Q. F. Dong, Z. G. Xiao, Y. B. Yuan and J. S. Huang, *Energy Environ. Sci.*, 2014, **7**, 2359–2365.
25 F. Hao, C. C. Stoumpos, Z. Liu, R. P. H. Chang and M. G. Kanatzidis, *J. Am. Chem. Soc.*, 2014, **136**, 16411–16419.
26 X. B. Xu, Z. H. Liu, Z. X. Zuo, M. Zhang, Z. X. Zhao, Y. Shen, H. P. Zhou, Q. Chen, Y. Yang and M. K. Wang, *Nano Lett.*, 2015, **15**, 2402–2408.

 This journal is © The Royal Society of Chemistry 2016

Published on 11 January 2016. Downloaded by HK University of Science and Technology on 23/03/2018 06:13:55.

27 Z. H. Wei, H. N. Chen, K. Y. Yan and S. H. Yang, *Angew. Chem., Int. Ed.*, 2014, **53**, 13239–13243.
28 F. Q. Zhang, X. C. Yang, H. X. Wang, M. Cheng, J. H. Zhao and L. C. Sun, *ACS Appl. Mater. Interfaces*, 2014, **6**, 16140–16146.
29 Z. Li, S. A. Kulkarni, P. P. Boix, E. Z. Shi, A. Y. Cao, K. W. Fu, S. K. Batabyal, J. Zhang, Q. H. Xiong, L. H. Wong, N. Mathews and S. G. Mhaisalkar, *ACS Nano*, 2014, **8**, 6797–6804.
30 J. Cao, Y. M. Liu, X. J. Xiao, J. Yin, J. Li, B. Xu, Y. Z. Tan and N. F. Zheng, *J. Am. Chem. Soc.*, 2015, **137**, 10914–10917.
31 K. Y. Yan, Z. H. Wei, J. K. Li, H. N. Chen, Y. Yi, X. L. Zheng, X. Long, Z. L. Wang, J. N. Wang, J. B. Xu and S. H. Yang, *Small*, 2015, **11**, 2269–2274.
32 Z. W. Wu, S. Bai, J. Xiang, Z. C. Yuan, Y. G. Yang, W. Cui, X. Y. Gao, Z. Liu, Y. Z. Jin and B. Q. Sun, *Nanoscale*, 2014, **6**, 10505–10510.
33 M. Batmunkh, C. J. Shearer, M. J. Biggs and J. G. Shapter, *J. Mater. Chem. A*, 2015, **3**, 9020–9031.
34 H. Chen, Z. Wei, X. Zheng and S. Yang, *Nano Energy*, 2015, **15**, 216–226.
35 M. Hu, L. F. Liu, A. Y. Mei, Y. Yang, T. F. Liu and H. W. Han, *J. Mater. Chem. A*, 2014, **2**, 17115–17121.
36 K. Cao, J. Cui, H. Zhang, H. Li, J. K. Song, Y. Shen, Y. B. Cheng and M. K. Wang, *J. Mater. Chem. A*, 2015, **3**, 9116–9122.
37 L. F. Liu, A. Y. Mei, T. F. Liu, P. Jiang, Y. S. Sheng, L. J. Zhang and H. W. Han, *J. Am. Chem. Soc.*, 2015, **137**, 1790–1793.
38 H. W. Zhou, Y. T. Shi, K. Wang, Q. S. Dong, X. G. Bai, Y. J. Xing, Y. Du and T. L. Ma, *J. Phys. Chem. C*, 2015, **119**, 4600–4605.
39 X. Y. Wang, Z. Li, W. J. Xu, S. A. Kulkarni, S. K. Batabyal, S. Zhang, A. Y. Cao and L. H. Wong, *Nano Energy*, 2015, **11**, 728–735.
40 W. J. Ke, G. J. Fang, Q. Liu, L. B. Xiong, P. L. Qin, H. Tao, J. Wang, H. W. Lei, B. R. Li, J. W. Wan, G. Yang and Y. F. Yan, *J. Am. Chem. Soc.*, 2015, **137**, 6730–6733.
41 H. H. Wang, Q. Chen, H. P. Zhou, L. Song, Z. St Louis, N. De Marco, Y. H. Fang, P. Y. Sun, T. B. Song, H. J. Chen and Y. Yang, *J. Mater. Chem. A*, 2015, **3**, 9108–9115.
42 N. J. Jeon, J. H. Noh, Y. C. Kim, W. S. Yang, S. Ryu and S. Il Seol, *Nat. Mater.*, 2014, **13**, 897–903.
43 E. Edri, S. Kirmayer, A. Henning, S. Mukhopadhyay, K. Gartsman, Y. Rosenwaks, G. Hodes and D. Cahen, *Nano Lett.*, 2014, **14**, 1000–1004.
44 T. Salim, S. Y. Sun, Y. Abe, A. Krishna, A. C. Grimsdale and Y. M. Lam, *J. Mater. Chem. A*, 2015, **3**, 8943–8969.
45 S. Aharon, S. Gamliel, B. El Cohen and L. Etgar, *Phys. Chem. Chem. Phys.*, 2014, **16**, 10512–10518.
46 Y. X. Zhao, A. M. Nardes and K. Zhu, *J. Phys. Chem. Lett.*, 2014, **5**, 490–494.
47 T. Leijtens, B. Lauber, G. E. Eperon, S. D. Stranks and H. J. Snaith, *J. Phys. Chem. Lett.*, 2014, **5**, 1096–1102.
48 M. T. Horantner, W. Zhang, M. Saliba, K. Wojciechowski and H. J. Snaith, *Energy Environ. Sci.*, 2015, **8**, 2041–2047.
49 Y. Li, X. Z. Ye, Y. R. Ma and L. M. Qi, *Small*, 2015, **11**, 1183–1188.
50 S. Y. Chen, Y. T. Yen, Y. Y. Chen, C. S. Hsu, Y. L. Chueh and L. J. Chen, *RSC Adv.*, 2012, **2**, 1314–1317.
51 P. Q. Gao, H. Z. Wang, Z. X. Sun, W. Q. Han, J. S. Li and J. C. Ye, *Appl. Phys. Lett.*, 2013, **103**, 253105.
52 S. H. Zhong, Z. G. Huang, X. X. Lin, Y. Zeng, Y. C. Ma and W. Z. Shen, *Adv. Mater.*, 2015, **27**, 555–561.
53 Y. C. Qiu, S. F. Leung, Q. P. Zhang, C. Mu, B. Hua, H. Yan, S. H. Yang and Z. Y. Fan, *Sci. Bull.*, 2015, **60**, 109–115.
54 S. Deki, Y. Aoi, Y. Asaoka, A. Kajinami and M. Mizuhata, *J. Mater. Chem.*, 1997, **7**, 733–736.
55 H. N. Chen, Z. H. Wei, K. Y. Yan, Y. Yi, J. N. Wang and S. H. Yang, *Faraday Discuss.*, 2014, **176**, 271–286.
56 C.-G. Wu, C.-H. Chiang, Z.-L. Tseng, M. K. Nazeeruddin, A. Hagfeldt and M. Gratzel, *Energy Environ. Sci.*, 2015, **8**, 2725–2733.
57 Y. H. Yu, J. Y. Li, D. L. Geng, J. L. Wang, L. S. Zhang, T. L. Andrew, M. S. Arnold and X. D. Wang, *ACS Nano*, 2015, **9**, 564–572.
58 D. W. deQuilettes, S. M. Vorpahl, S. D. Stranks, H. Nagaoka, G. E. Eperon, M. E. Ziffer, H. J. Snaith and D. S. Ginger, *Science*, 2015, **348**, 683–686.
59 W. Y. Nie, H. H. Tsai, R. Asadpour, J. C. Blancon, A. J. Neukirch, G. Gupta, J. J. Crochet, M. Chhowalla, S. Tretiak, M. A. Alam, H. L. Wang and A. D. Mohite, *Science*, 2015, **347**, 522–525.
60 J. Burschka, N. Pellet, S. J. Moon, R. Humphry-Baker, P. Gao, M. K. Nazeeruddin and M. Gratzel, *Nature*, 2013, **499**, 316–319.
61 D. Y. Liu, M. K. Gangishetty and T. L. Kelly, *J. Mater. Chem. A*, 2014, **2**, 19873–19881.
62 H. J. Snaith, A. Abate, J. M. Ball, G. E. Eperon, T. Leijtens, N. K. Noel, S. D. Stranks, J. T. W. Wang, K. Wojciechowski and W. Zhang, *J. Phys. Chem. Lett.*, 2014, **5**, 1511–1515.
63 J. D. Chen, C. H. Cui, Y. Q. Li, L. Zhou, Q. D. Ou, C. Li, Y. F. Li and J. X. Tang, *Adv. Mater.*, 2015, **27**, 1035–1041.
64 H. Y. Wei, J. H. Huang, C. Y. Hsu, F. C. Chang, K. C. Ho and C. W. Chu, *Energy Environ. Sci.*, 2013, **6**, 1192–1198.
65 H. K. Raut, V. A. Ganesh, A. S. Nair and S. Ramakrishna, *Energy Environ. Sci.*, 2011, **4**, 3779–3804.
66 J. G. Cai and L. M. Qi, *Mater. Horiz.*, 2015, **2**, 37–53.
67 S. J. Ha and J. H. Moon, *Sci. Rep.*, 2014, **4**, 5375.
68 S. F. Leung, Q. P. Zhang, F. Xiu, D. L. Yu, J. C. Ho, D. D. Li and Z. Y. Fan, *J. Phys. Chem. Lett.*, 2014, **5**, 1479–1495.
69 Q. F. Lin, S. F. Leung, L. F. Lu, X. Y. Chen, Z. Chen, H. N. Tang, W. J. Su, D. D. Li and Z. Y. Fan, *ACS Nano*, 2014, **8**, 6484–6490.
70 P. Loper, M. Stuckelberger, B. Niesen, J. Werner, M. Filipic, S. J. Moon, J. H. Yum, M. Topic, S. De Wolf and C. Ballif, *J. Phys. Chem. Lett.*, 2015, **6**, 66–71.
71 L. A. Fielding, O. O. Mykhaylyk, A. Schmid, D. Pontoni, S. P. Armes and P. W. Fowler, *Chem. Mater.*, 2014, **26**, 1270–1277.
72 J. Ferber and J. Luther, *Sol. Energy Mater. Sol. Cells*, 1998, **54**, 265–275.

Published on 11 January 2016. Downloaded by HK University of Science and Technology on 23/03/2018 06:13:55.

73 C. Cheng, M. M. Lee, N. K. Noel, G. M. Hughes, J. M. Ball, H. E. Assender, H. J. Snaith and A. A. R. Watt, *ACS Appl. Mater. Interfaces*, 2014, **6**, 14247–14252.
74 S. Hore, P. Nitz, C. Vetter, C. Prahl, M. Niggemann and R. Kern, *Chem. Commun.*, 2005, 2011–2013.
75 J. W. Lee, J. Lee, C. Kim, C. Y. Cho and J. H. Moon, *Sci. Rep.*, 2014, **4**, 6804.
76 X. Chen, S. Yang, Y. C. Zheng, Y. Chen, Y. Hou, X. H. Yang and H. G. Yang, *Adv. Sci.*, 2015, **2**, 1500105.
77 A. Listorti, E. J. Juarez-Perez, C. Frontera, V. Roiati, L. Garcia-Andrade, S. Colella, A. Rizzo, P. Ortiz and I. Mora-Sero, *J. Phys. Chem. Lett.*, 2015, **6**, 1628–1637.
78 D. Shi, V. Adinolfi, R. Comin, M. J. Yuan, E. Alarousu, A. Buin, Y. Chen, S. Hoogland, A. Rothenberger, K. Katsiev, Y. Losovyj, X. Zhang, P. A. Dowben, O. F. Mohammed, E. H. Sargent and O. M. Bakr, *Science*, 2015, **347**, 519–522.
79 W. Zhang, M. Saliba, S. D. Stranks, Y. Sun, X. Shi, U. Wiesner and H. J. Snaith, *Nano Lett.*, 2013, **13**, 4505–4510.
80 K. Wang, Y. T. Shi, Q. S. Dong, Y. Li, S. F. Wang, X. F. Yu, M. Y. Wu and T. L. Ma, *J. Phys. Chem. Lett.*, 2015, **6**, 755–759.
81 V. Gonzalez-Pedro, E. J. Juarez-Perez, W.-S. Arsyad, E. M. Barea, F. Fabregat-Santiago, I. Mora-Sero and J. Bisquert, *Nano Lett.*, 2014, **14**, 888–893.
82 P. Tiwana, P. Docampo, M. B. Johnston, H. J. Snaith and L. M. Herz, *ACS Nano*, 2011, **5**, 5158–5166.
83 A. K. Chandiran, M. Abdi-Jalebi, M. K. Nazeeruddin and M. Gratzel, *ACS Nano*, 2014, **8**, 2261–2268.

This journal is © The Royal Society of Chemistry 2016